AGU PUBLICATIONS

JGR

Journal of Geophysical Research: Space Physics

RESEARCH ARTICLE
10.1002/2016JA022613

Key Points:
- Scintillations due to a BT 1 blob are higher than the corresponding polar cap patch
- BT 2 blobs produced by auroral precipitation only give rise to minor GNSS scintillations
- Soft particle precipitation is unlikely to be the main source of the enhanced scintillation at nighttime

Supporting Information:
- Supporting Information S1
- Movie S1

Correspondence to:
Y. Jin,
yaqi.jin@fys.uio.no

Citation:
Jin, Y., J. I. Moen, W. J. Miloch, L. B. N. Clausen, and K. Oksavik (2016), Statistical study of the GNSS phase scintillation associated with two types of auroral blobs, *J. Geophys. Res. Space Physics*, *121*, doi:10.1002/2016JA022613.

Received 26 FEB 2016
Accepted 19 APR 2016
Accepted article online 21 APR 2016

Statistical study of the GNSS phase scintillation associated with two types of auroral blobs

Yaqi Jin[1], Jøran I. Moen[1,2], Wojciech J. Miloch[1], Lasse B. N. Clausen[1], and Kjellmar Oksavik[2,3]

[1]Department of Physics, University of Oslo, Oslo, Norway, [2]University Centre in Svalbard, Longyearbyen, Norway, [3]Birkeland Centre for Space Science, Department of Physics and Technology, University of Bergen, Bergen, Norway

Abstract This study surveys space weather effects on GNSS (Global Navigation Satellite System) signals in the nighttime auroral and polar cap ionosphere using scintillation receivers, all-sky imagers, and the European Incoherent Scatter Svalbard radar. We differentiate between two types of auroral blobs: blob type 1 (BT 1) which is formed when islands of high-density *F* region plasma (polar cap patches) enter the nightside auroral oval, and blob type 2 (BT 2) which are generated locally in the auroral oval by intense particle precipitation. For BT 1 blobs we have studied 41.4 h of data between November 2010 and February 2014. We find that BT 1 blobs have significantly higher scintillation levels than their corresponding polar cap patch; however, there is no clear relationship between the scintillation levels of the preexisting polar cap patch and the resulting BT 1 blob. For BT 2 blobs we find that they are associated with much weaker scintillations than BT 1 blobs, based on 20 h of data. Compared to patches and BT 2 blobs, the significantly higher scintillation level for BT 1 blobs implies that auroral dynamics plays an important role in structuring of BT 1 blobs.

1. Introduction

Plasma irregularities can affect transionospheric electromagnetic signals and cause rapid fluctuations of the received wave amplitude and phase on the ground, which are often referred to as scintillations [see, e.g., *Yeh and Liu*, 1982; *Kintner et al.,* 2007]. Studies on ionospheric scintillations started early [*Hey et al.,* 1946], and subsequent research revealed that ionospheric scintillations frequently occurred in the equatorial region and at high latitudes [*Fremouw et al.,* 1978; *Kelley et al.,* 1980; *Yeh and Liu*, 1982; *Aarons*, 1982; *Aarons et al.,* 1983; *Buchau et al.,* 1985; *Basu et al.,* 1988, 2002; *Basu and Groves*, 2001]. Due to increasing human activity in the polar regions, there is a growing number of scintillation studies in the Arctic, particularly in terms of the GNSS (Global Navigation Satellite System) scintillation [*Mitchell et al.,* 2005; *Prikryl et al.,* 2010; *Moen et al.,* 2013; *Andalsvik and Jacobsen*, 2014; *Jin et al.,* 2014, 2015; *van der Meeren et al.,* 2014, 2015; *Oksavik et al.,* 2015]. It has been found that GPS (Global Positioning System) phase scintillations dominate over GPS amplitude scintillations at high latitudes [e.g., *Spogli et al.,* 2009; *Prikryl et al.,* 2011].

Since ionospheric scintillations are caused by ionospheric plasma irregularities, scintillation studies can also reveal possible sources of the irregularities. A number of mechanisms have been proposed to explain the irregularity production at high latitudes [*Keskinen and Ossakow*, 1983; *Keskinen et al.,* 1988; *Tsunoda*, 1988; *Kelley et al.,* 1982], including plasma turbulence [*Huba et al.,* 1985; *Kintner and Seyler*, 1985], the gradient drift instability (GDI) [*Keskinen and Ossakow*, 1983; *Gondarenko and Guzdar*, 2004], the Kelvin-Holmholtz instability (KHI, or velocity shear-driven instability) [*Keskinen et al.,* 1988; *Basu et al.,* 1990], the temperature gradient instability [*Hudson and Kelley*, 1976], and the current-convective instability (CCI) [*Ossakow and Chaturvedi*, 1979]. The GDI has been adapted to include the effect of CCI, which occurs principally in the downward field-aligned current (FAC) region [*Tsunoda*, 1988]. *Carlson* [2012] proposed a two-step KHI-GDI process, where the KHI speed up the GDI process by generating seed irregularities for the GDI process. It is nontrivial to quantify the instability growth rates of plasma irregularities, and in situ measurements are crucial [*Moen et al.,* 2002, 2012; *Oksavik et al.,* 2012; *Spicher et al.,* 2015a].

Recently, *Jin et al.* [2015] demonstrated that strong scintillations are well colocated with the auroral zone around noon and related this to particle precipitation, such as the poleward moving auroral form (PMAF). In a case study, *Oksavik et al.* [2015] presented that severe scintillations and the loss of signal lock were associated with two PMAFs. In general, in the European Arctic region, strong phase scintillations are more frequently observed around magnetic midnight as compared to the daytime [*Jin et al.,* 2015].

The IMF (interplanetary magnetic field) driven transport of polar cap patches from day to night is a significant space weather phenomenon [*Foster et al.,* 2005; *Oksavik et al.,* 2010; *Zhang et al.,* 2013, 2015]. During the polar night, in the dark polar cap winter condition, polar cap patches can be tracked using the ASI (all-sky imager) and MSP (meridian scanning photometer) [*Buchau et al.,* 1985; *Weber et al.,* 1986; *Lorentzen et al.,* 2004; *Moen et al.,* 2007, 2015; *Hosokawa et al.,* 2009, 2011]. The monitoring emission line results from the atomic oxygen at a wavelength of 630.0 nm during the recombination process of the dominant O^+ ion [see, e.g., *Hosokawa et al.,* 2011]. There are several studies showing that airglow patches exit the polar cap and enter the auroral region [*Lorentzen et al.,* 2004; *Moen et al.,* 2007]. *Moen et al.* [2007] showed that 60% of patches exit the polar cap between 22 and 01 MLT (magnetic local time), but the entire distribution spans from 18:30 MLT to 04:50 MLT. Polar cap patches of high-density *F* region plasma exit the polar cap into the nighttime aurora and then return to the dayside [*Crowley et al.,* 2000; *Zhang et al.,* 2013, 2015].

When patches that exit the polar cap are inside the auroral oval, they are termed auroral blobs. Although blobs have been studied for more than three decades [*Vickrey et al.,* 1980; *Kelley et al.,* 1982; *Rino et al.,* 1983; *Weber et al.,* 1985; *Basu et al.,* 1990; *Tsunoda*, 1988; *Crowley et al.,* 2000], there is still no unanimous definition of a blob. In this study, we will differentiate between two types of auroral blobs: blob type 1 (BT-1) is connected to the high-density polar cap patch material that has entered the auroral oval; and blob type-2 (BT-2) relates to the plasma density enhancement/structure that has been generated locally by particle precipitation.

Jin et al. [2014] showed that in the European Arctic sector, the worst scintillation case is the BT-1 blob. In a case study, *van der Meeren et al.* [2015] confirmed that the strongest scintillations were found at the poleward edge of the nightside auroral oval when the polar cap patches were pulled into the nightside auroral region. In a superposed epoch analysis of the GPS scintillation, it is found that at night the scintillation region locates in the auroral region as inferred from the simultaneous FAC data from AMPERE satellites [*Clausen et al.,* 2016]. They also demonstrated a connection between high scintillation region and the upward FAC in the dawnside and duskside.

The statistics of scintillations with respect to the nightside aurora was studied with the statistical auroral oval [e.g., *Spogli et al.,* 2009; *Prikryl et al.,* 2011] or with FAC data from AMPERE which were used as a reference for the oval [*Clausen et al.,* 2016]. These previous works could not study in detail the scintillations with respect to the actual location of the auroral oval. So far there has not been any statistical work based on GNSS scintillation data and auroral imaging at night. For both scientific understanding and for the practical side of space weather monitoring, it is however crucial to identify what the actual source of the strong scintillations is and to determine the relative importance of polar cap patches, blobs, and auroral precipitation. In this study, we make use of an airglow ASI and a colocated GNSS scintillation receiver to carry out such a statistical study and address the question of blob scintillation using a large data set.

The paper is organized as follows. Section 2 briefly introduces the instrumentation. Section 3.1 presents a scintillation case associated with BT-1 blobs (due to polar cap patches + auroras), while section 3.2 shows a case for BT-2 blobs (due to auroral precipitation without patches). Section 4 presents statistical results from 41.4 h of data spanned between November 2010 and February 2014 when patches were pulled into the nightside aurora (BT-1 blobs) and 20 h of data in nightside aurora without patches (BT-2 blobs). The possible instability modes and the role of soft particle precipitation are discussed in section 5, followed by a short summary in section 6.

2. Instrumentation

Instruments that are used in this study include ASIs in Ny-Ålesund and Longyearbyen, GNSS scintillation receivers in Ny-Ålesund and Longyearbyen, the European Incoherent Scatter (EISCAT) Svalbard Radar (ESR), and magnetometers in Longyearbyen. In addition, the OMNI IMF data are used.

The ASI in Ny-Ålesund (named NYA4) was located at Sverdrup Research Station (78.9°N, 11.9°E; 76.6° MLAT, 24:00 MLT = 20:50 UT). The NYA4 ASI used an EMCCD (electron multiplying charge-coupled device). The ASI in Longyearbyen (named LYR5) is located at Kjell Henriksen Observatory (KHO; 78.2°N, 16.0°E; 75.4° MLAT). The LYR5 ASI uses an ICCD (intensified charge-coupled device). Ny-Ålesund is 113 km northwest of Longyearbyen, and the two stations are roughly on the same magnetic meridian line. Both imagers record emission intensity across the sky with a 180° field of view fish eye lens at 630.0 nm every 30 s and 557.7 nm

every 15 s, respectively. The intensity of both ASIs are calibrated into the standard kilo Rayleigh (kR) intensity scale, but the NYA4 ASI saturates at ~9 kR in the 557.7 nm channel, which may underestimate the intensity of the substorm auroral activity. The NYA4 ASI was operated from October 2010 to March 2014, and it was moved to another site in October 2014. The LYR5 ASI has been operated since January 2013. Both ASIs are able to track airglow patches, but NYA4 ASI data were used for the statistical study of scintillations because of its longer operation time. Data from both ASIs are cut at the elevation angle of 15° due to edge effects.

In addition to the 2-D images which show the horizontal structures of airglow patches and auroras, data from the ESR in Longyearbyen are used to monitor the electron density profile and other ionospheric parameters. The ESR consists of a 32 m steerable antenna and a 42 m static field-aligned antenna (azimuth = 184°, elevation = 82°). Both antennas allow for measurements of electron density, electron temperature, ion temperature, and line of sight ion velocity as a function of range. For this study, only data from the field-aligned antenna (42 m) are used.

In order to study the scintillation effect associated with the specific ionospheric phenomena, we use two GNSS scintillation receivers. The first GNSS receiver is located in Ny-Ålesund and is operated by the University of Oslo (UiO). The UiO GNSS scintillation receiver is the standard GNSS Ionospheric Scintillation/total electron content (TEC) Monitor (GISTM), model GSV4004B [*Van Dierendonck et al.,* 1993]. The carrier phase and power at the L1 frequency are tracked and recorded at 50 Hz rate. The phase (σ_ϕ) and amplitude scintillation indices (S_4) are also calculated and recorded automatically. The phase scintillation index is defined as the standard deviation of the carrier phase that has been detrended by the high-pass sixth-order Butterworth filter with a cutoff frequency of 0.1 Hz. The GPS TEC data have been postprocessed by using WinTEC-P [*Carrano et al.,* 2009]. The ROT (Rate of TEC) data over 1 min are also used to depict the TEC variations [see, e.g., *Alfonsi et al.,* 2011], where ROT = ΔTEC/Δt. The second GNSS receiver is located at KHO and is operated by the University of Bergen (UiB). This is a new type NovAtel GPStation-6 GISTM [*NovAtel*, 2012]. This receiver can track GPS, GLONASS, and Galileo satellites. However, for both receivers only data from GPS satellites are considered in this study. (For the scintillation case of GLONASS and Galileo systems, interested readers can refer to *van der Meeren et al.* [2015]). The UiB GNSS receiver is colocated with the LYR5 ASI in Longyearbyen, while the UiO GNSS receiver is colocated with the NYA4 ASI in Ny-Ålesund. In section 4 (statistical study), a cutoff elevation angle of 15° is used for the GPS scintillation data. The cutoff angle of 15° for the Ny-Ålesund stations was used in the case and statistical studies, and was found to be adequate to use [e.g., *Spogli et al.,* 2009; *Jin et al.,* 2014, 2015]. Due to the specific location of Ny-Ålesund station, this cutoff elevation angle is sufficient to minimize multipath effects.

The OMNI IMF data in GSM (geocentric solar magnetospheric) coordinates are used to present the upstream IMF condition [*King and Papitashvili*, 2005]. The 1 min resolution spacecraft-interspersed IMF data are from the OMNI web (the high-resolution OMNI data set) (http://omniweb.gsfc.nasa.gov/html/sc_merge_data1.html). The OMNI IMF data are already shifted from the observation points to the Earth's bow shock nose by using several time shift techniques.

We also use the *H* and *Z* components of the magnetic field which were measured at KHO in Longyearbyen. The magnetometer is operated by the University of Tromsø.

3. Case Study

3.1. BT-1 Blob: 1 February 2014

This event gives an example of the scintillation and ionospheric conditions associated with the formation of BT-1 blobs when the polar cap patches entered the auroral oval. An overview of this event is given in Figure 1. Figures 1a and 1b show the optical emission from the red line (630.0 nm, Figure 1a) and green line (557.7 nm, Figure 1b) from Ny-Ålesund on 1 February 2014, from 21–24 UT (0:10–3:10 MLT) in a keogram format as a function of scan angle from 15°N to 165°S. The emission intensity is shown in units of kilo Rayleigh. Note that the scales of the color bars are different for the two emission lines. The white horizontal lines in Figures 1a and 1b show approximately the location of the ESR beam for the assumed emission altitudes of 250 km and 120 km, respectively. These altitudes are the typical emission altitudes of the two emission lines [*van der Meeren et al.,* 2015; *Sandholt et al.,* 2002]. The blue color (<0.1 kR) in Figure 1a indicates the background. The polar cap airglow patches can be clearly seen as slightly bent vertical stripes in turquoise-yellow color

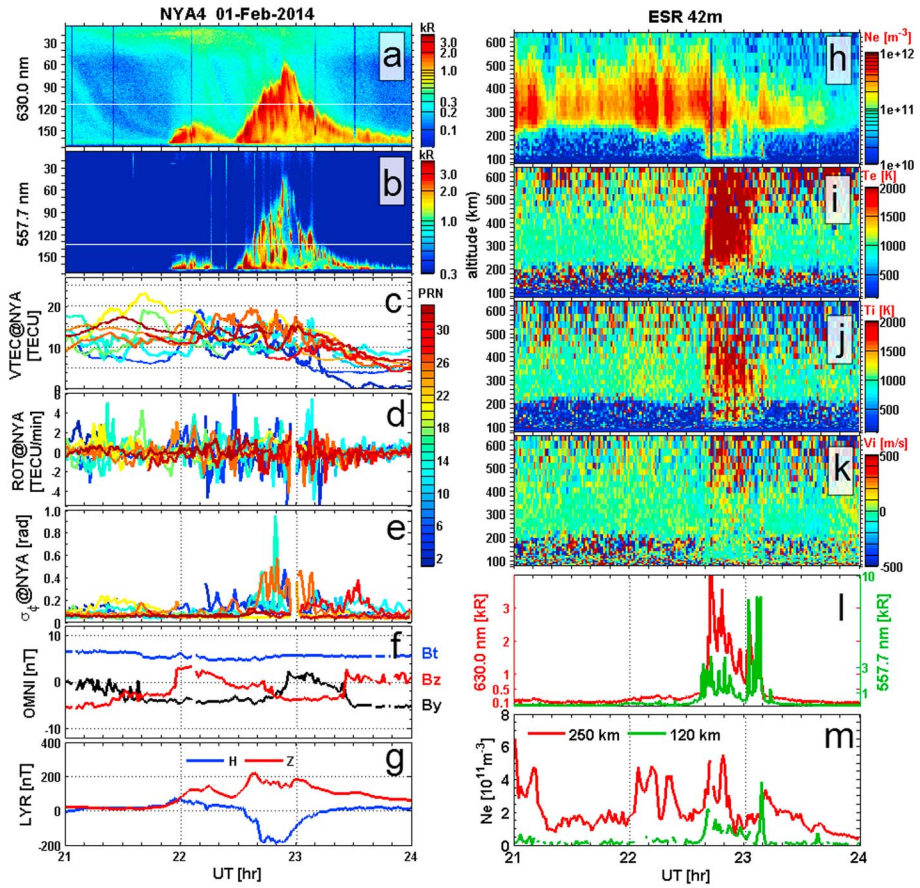

Figure 1. Event overview of the BT-1 case. (a and b) The keogram data derived from NYA4 all-sky imager in Ny-Ålesund at 630.0 nm and 557.7 nm as a function of the scan angle from 15°N to 165°S. The intensity is shown in kilo Rayleigh which is color coded on the right. The horizontal white lines indicate the location of the ESR beam. (c–e) The GPS vertical TEC (VTEC), ROT (Rate of TEC), and phase scintillation indices (σ_ϕ) from all tracked GPS satellites which are color coded on the right by their PRN code. (f) The IMF strength (B_t), B_y, and B_z from the OMNI data set. (g) The H and Z component of the magnetic field observed from Longyearbyen. (h–k) The electron density (N_e), electron temperature (T_e), ion temperature (T_i), and line of sight ion velocity (V_i, positive is away from the radar) observed from ESR 42 m antenna. (l) The optical emission above the ESR beam at 630.0 nm (in red) and 557.7 nm (in green). (m) The time series of electron density at 250 km and 120 km.

(~0.5 kR) which directed toward the bright auroral poleward boundary in red (>1 kR) and then BT-1 blobs were formed.

Before 21:52 UT, the auroral oval was equatorward of the southern horizon. The auroral oval expanded poleward into the field of view from 21:52 UT. This is the characteristic feature of a substorm expansion phase with ongoing tail reconnection [*Lorentzen et al.,* 2004]. The aurora attained its first maximum latitude at ~22:08 UT and then retreated equatorward. It expanded poleward again after 22:29 UT and covered the ESR beam at around 22:40 UT and continuously moved poleward until ~22:54 UT, then it gradually retreated equatorward and stayed equatorward of the ESR beam from 23:10 UT. The ESR beam was covered by the auroral precipitation for around 30 min. The substorm aurora is also clearly seen in the green line emission (Figure 1b). During the poleward expansion and equatorward leap, the poleward boundary of the aurora brightened quasiperiodically, which is called poleward boundary intensification (PBI) [see, e.g., *Zesta et al.,* 2002]. Auroral streamers formed from the PBI and tilted southward and moved equatorward; this can be seen from Figures 1a and 1b inside the auroral region (for more detailed auroral morphology, see Movie S1 in the supporting information). The poleward boundary of the nightside aurora can be seen as a proxy of the open closed field line boundary (OCB) [*Blanchard et al.,* 1995; *Lorentzen et al.,* 2004; *Moen et al.,* 2007, 2015]. The airglow polar cap patches were pulled across the OCB into the auroral region by the background convection flow where they are termed BT-1 blobs (see also Movie S1).

The GNSS scintillation receiver at Ny-Ålesund is used to monitor the scintillation condition during this event. Figures 1c–1e show the GPS vertical TEC (VTEC), ROT, and phase scintillation index (σ_ϕ) from all available GPS satellites. The GPS satellites are color coded by their PRN (Pseudo Random Noise) code given in the color bar. The GPS TEC shows very clear variations between 10 and 20 TECU from 21:00 to 23:30 UT which indicate the passage of polar cap patches. After 23:20 UT, the TEC decreased gradually to below 10 TECU. This is consistent with the 630.0 nm airglow measurements, which show a decrease in the airglow emission intensity, too. The TEC variation can also be seen from the ROT data in Figure 1d, which shows fluctuations up to 6 TECU/min from 21:00 UT to 23:20 UT followed by a sudden drop of the fluctuation level, consistent with the TEC measurements. The GPS phase scintillation was generally low (below 0.3 rad) before 22:40 UT and intensified when the aurora reached the scan angle of ~120°. The enhanced scintillation lasted until 23:10 UT.

Figure 1f shows the IMF strength B_t, and its components B_y and B_z from the OMNI data set. The IMF strength was rather stable during this time. The IMF B_y was mainly negative with a brief positive excursion ~23:00 UT. The IMF B_z was negative from 21:00 to 21:55 UT, followed by a quick northward variation and became southward from 22:20 UT to 23:25 UT. From 23:30 to 24:00 UT, the IMF B_z was nearly 0. Negative B_z favors the production of polar cap patches and the substorm activity.

The local magnetic signature of the substorm is also shown in Figure 1g which presents the H and Z components of the ground-based magnetic measurements from Longyearbyen (LYR). The magnetic data can be used as a measure of the substorm electrojet and the evolution of a substorm. The magnetic field was generally quiet before 21:50 UT. Then the H component first slightly increased and then gradually decreased until 22:30 UT. This was consistent with the first auroral poleward expansion shown in Figure 1a. From 22:30 UT to 22:50 UT, the H component decreased very sharply down to nearly −200 nT. The rapid negative deflection of H was consistent with the second rapid poleward expansion of the substorm aurora. The H component recovered to a stable value at 23:30 UT. The Z component was positive and showed several impulses, which were associated with variations of the H component. The positive Z component indicates that the major substorm electrojet was equatorward of the magnetometer station.

In order to discuss the detailed ionospheric conditions during this event, we show in Figures 1h–1k ionospheric parameters (electron density N_e, electron temperature T_e, ion temperature T_i, and ion velocity V_i) from 21:00 to 24:00 UT as observed by the ESR which was pointing along the magnetic field line. Figure 1h shows a sequence of typical polar cap patches with electron densities up to 5×10^{11} m^{-3}. The enhanced density ranged from 200 km to 500 km. The ESR beam encountered aurora from 22:40 UT to 23:10 UT, during which time the precipitating particles ionized the ionosphere. The enhanced particle ionization was seen from 200 km down to 100 km, which corresponds to precipitating electron energies between 1 keV and 30 keV [*Rees*, 1963]. While the precipitation affected the electron density below 200 km, the enhanced electron temperature was clearer above 200 km (F region). The enhanced ion temperature (T_i) was visible down to around 120 km, but it was clearer above 200 km. The ion upflow was recorded above 400 km, which was indicated by the positive (upward) ion velocity.

To better coordinate observations from the ESR and NYA4 ASI, we present in Figure 1l the optical emissions at the location of the ESR beam (the horizontal white line in Figures 1a and 1b) and the ESR observed electron density in Figure 1m. Figure 1l shows emissions of 630.0 nm (in red) and 557.7 nm (in green) at the location of the ESR beam. The intensified auroral emission was seen from 22:40 UT to 23:10 UT as the aurora covered the ESR beam. Figure 1m shows the electron density at altitudes of 120 km (in green) and 250 km (in red). The data from other altitudes can be found in the Supporting Information S1. The variation of the electron density at 250 km ($0.5–6 \times 10^{11}$ m^{-3}) indicates the passage of polar cap patches, and the auroral particle precipitation did not affect the electron density at this altitude. The electron density at 120 km was very low ($N_e < 0.5 \times 10^{11}$ m^{-3}) before 22:40 UT and was enhanced by the auroral electron precipitation to above 10^{11} m^{-3} during the auroral coverage.

With background ionospheric conditions given above, we now elaborate on the scintillation condition during the second poleward expansion and equatorward retreat of the substorm aurora (from 22:30 UT to 23:30 UT). Figures 2a–2f show a sequence of optical images from the NYA4 ASI in Ny-Ålesund. The emission intensity is color coded in a log scale as given in the color bar on the left side of Figure 2a. In Figures 2a–2f, the images are shown in the azimuth and elevation format, where the geographic north is up and west is to the left. Thus, the GPS satellite locations were also overlaid onto each image using the azimuth and elevation angles [see, e.g.,

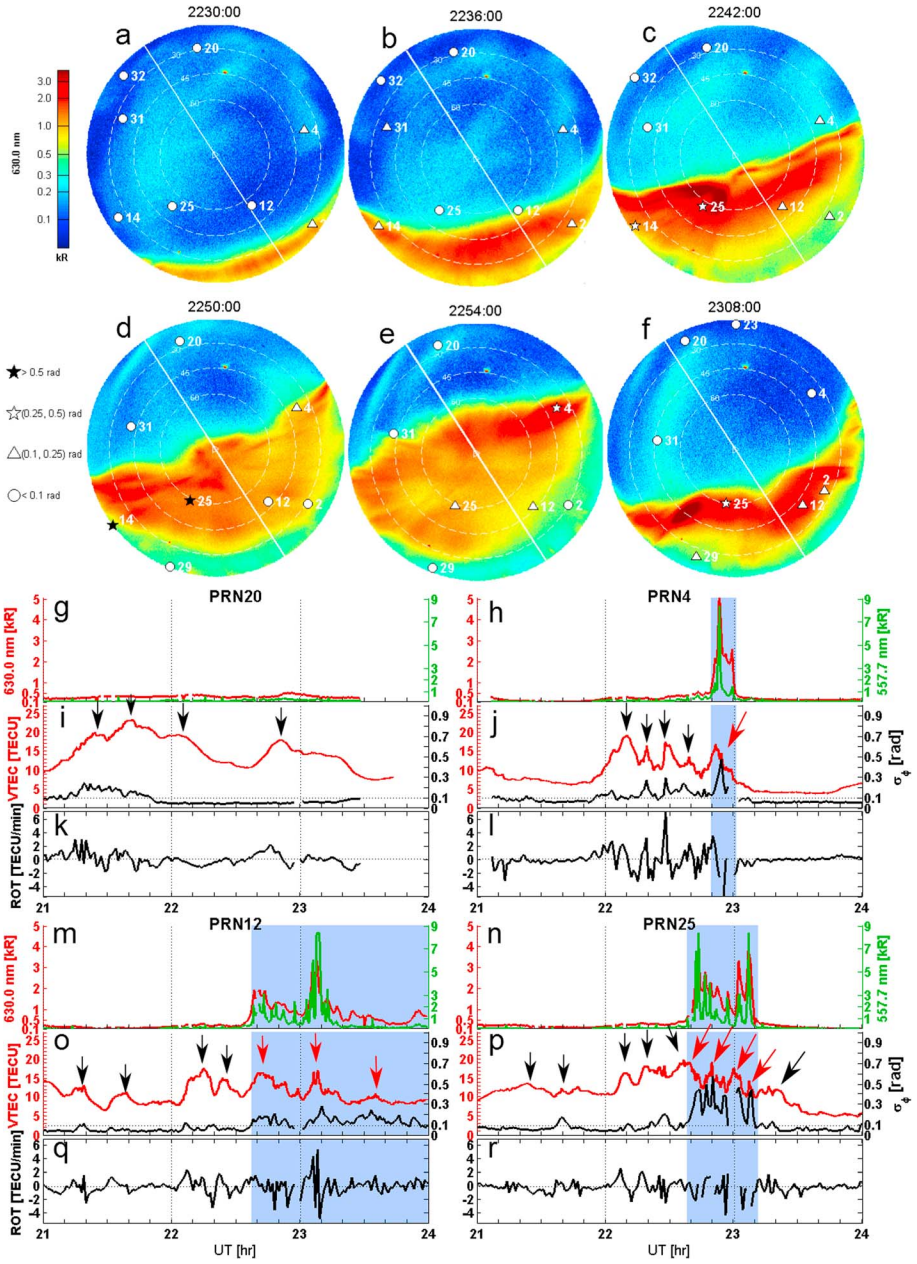

Figure 2. (a–f) A sequence of snapshots showing that airglow polar cap patches were pulled into the nightside auroral region. The data are from the 630.0 nm channel. The intensity of the emission is shown in the color bar on the left of Figure 2a. The magnetic meridian line above the station is plotted in slant white solid line. In Figures 2a–2f, the optical data are presented in the azimuth and elevation angle format. The geographic north is up and west is to the left. The elevation angle at 30°, 45°, and 60° are plotted in white dashed circles. GPS satellites are superimposed onto the images using the azimuth and elevation angles of each satellite and are annotated by the PRN code. The symbols (circle, triangle, star, and black star) refer to different phase scintillation levels as shown on the left side of Figure 2d. (g–r) Optical emissions, the GPS TEC, ROT, and phase scintillation index for four selected satellites (see text for more details). Note that Figures 2k–2l and 2q–2r use the same vertical axis.

Jin et al., 2014]. Eight GPS satellites were tracked at this time that had elevation angle larger than 15°. GPS satellites are annotated by their PRN code. The symbols refer to different phase scintillation levels as shown on the left side of Figure 2d.

Figure 2a was taken at 22:30 UT when the aurora started to leap poleward from the scan angle of 150° in agreement with Figure 1a. The aurora continued moving poleward and reached 130° in Figure 2b and

100° in Figure 2c. The poleward boundary of the aurora intensified (i.e., PBI occurred) during this poleward expansion. The aurora reached the zenith (90°) of Ny-Ålesund at around 22:50 UT and attained its highest latitude at 22:54 UT as shown in Figure 2e. After the maximum poleward expansion, the aurora started to retreat equatorward. During poleward and equatorward motions, the aurora was more intense in the poleward portion.

The airglow patches can be clearly seen poleward of the OCB. The patches moved southward to meet the auroral boundary and formed the BT-1 blobs equatorward of the auroral boundary. The airglow was enhanced in Figure 2c when the auroral boundary moved to 100°. This was possibly due to enhanced convection, which pulled the ionosphere slightly downward because the $\mathbf{E} \times \mathbf{B}$ drift has a slightly downward component at night [*Perry et al.,* 2013]. After 22:50 UT, the patches were mainly seen in the western part of the field of view. This was because the ASI moved with the Earth to the dawnside of the midnight convection throat [*Moen et al.,* 2015]. In Figure 2d, the diffuse patchy structures disappeared and the large-scale elongated structures (cigar shaped) dominated. This cigar shaped structures are even clearer in Figures 2e and 2f. The airglow patches were seen to convect into the auroral region during both the poleward expansion (Figures 2a–2e) and equatorward retreat (Figure 2d) of the auroral boundary. An animation of the 630.0 nm and 557.7 nm image sequences from 21:55–23:29 UT is provided in the supporting information Movie S1.

The GPS TEC, ROT, and σ_ϕ along with the optical emissions near the satellite locations from four selected GPS satellites are shown as time series in Figures 2g–2r in the same manner as Figures 1l and 1m at the ESR location. Figures 2g–2h and 2m–2n show the 630.0 nm (in red) and 557.7 nm (in green) optical emissions near the locations of the satellites. The locations of satellites were projected by using the azimuth and elevation angles. The vertical axes are shown in the log scale in order to better present both airglow patches ($\leq$0.5 kR) and auroral intensity ($>$1 kR). The GPS satellites are moving very slowly (~100 m/s) compared to the polar cap patches and auroras, so the GPS satellites can be seen as quasi-stationary in a short period. Figures 2i–2j and 2o–2p show the GPS vertical TEC (in red) and phase scintillation index (in black) for each satellite. The TEC humps, which were signatures of polar cap patches or substructures inside them passing through the ray paths, are annotated by black arrows. The shaded regions refer to the time when the aurora intersected with the ray paths of the satellites. Figures 2k–2l, and 2q–2r show the corresponding ROT data.

3.1.1. Satellite PRN20

PRN20 was located in the northern part of the field of view and moved slowly westward. Because PRN20 was far north, the aurora did not intersect with its ray path which can be seen from the low values of 630.0 nm and 557.7 nm emission in Figure 2g. Therefore, PRN20 presents the scintillation condition associated with polar cap patches only. The TEC variation in Figure 2i indicated the passage of a sequence of polar cap patches. Figure 2k presents the ROT activity associated with these polar cap patches. Note that the first three TEC humps may be substructures of one polar cap patch according to the definition, i.e., with density twice higher than the background. Only the first two TEC humps (from 21:10 UT to 21:50 UT) were associated with phase scintillations. While the trailing part (marked by the third black arrow) of the patch was not associated with phase scintillations, although Figure 2k presents a smooth negative ROT variation (decreasing TEC). The phase scintillation index remained at the noise level (~0.05 rad) after 21:50 UT although another patch (annotated by the last black arrow) passed through the ray path. The 630.0 nm emission was very low and the variation was less clear than the TEC variation. But the emission was enhanced after 22:50 UT. This was possibly due to the enhanced convection flow (see the airglow changes between Figures 2b and 2c). The 557.7 nm emission was very low throughout the period.

3.1.2. Satellite PRN4

Figures 2h, 2j, and 2l show measurements associated with PRN4. PRN4 was in the eastern part of the field of view and moved slowly northward. The TEC was very smooth before around 21:50 UT. Four TEC humps were seen between 21:50 UT and 22:47 UT which may be substructures of one polar cap patch, and the associated phase scintillations were observed up to 0.26 rad. The associated ROT value went up to 7 TECU/min. The aurora passed through the ray path of PRN4 from 22:49 UT to 23:01 UT (shaded region) as seen from Figure 2h. The auroral intensity reached up to 5 kR for 630.0 nm and 8 kR for 557.7 nm. The TEC peak within the auroral precipitation region is marked with the red arrow, which is per definition a BT-1 blob. The enhanced scintillation (up to 0.45 rad) was seen at the trailing edge of this blob and the scintillation peak occurred slightly after the peak in the auroral intensity. It is unclear whether the scintillation favors the trailing edge or whether this is due to the finite response time in irregularity growth. But since there was a data gap

around 23:00 UT, we cannot tell whether there was a higher or lower scintillation with the second weaker 557.7 nm emission pulse.

3.1.3. Satellite PRN12

Figures 2m, 2o, and 2q show measurements associated with PRN12. PRN12 was in the southern part of the ASI field of view at a high elevation angle (60°) at 22:10 UT and slowly moved eastward. The poleward boundary of the aurora intersected with the ray path at around 22:37 UT during the auroral poleward expansion. Then the poleward boundary intersected with the ray path at around 23:08 UT when the aurora retreated equatorward (see Figure 2f). As the aurora retreated equatorward to south of 150° scan angle (after 23:30 UT) and PRN12 moved to the southeast edge of the field of view to catch up with the aurora, the sequence of auroral brightenings in the southern field of view affected PRN12. This active region is shaded in Figures 2m, 2o, and 2q. Figure 2o shows four humps in TEC which are marked with black arrows before 22:37 UT, the associated ROT varied between −3 TECU/min to 2 TECU/min, but the scintillations associated with these TEC humps were very low (≤0.1 rad). Two strong BT-1 blobs (high TEC value) and one weak BT-1 blob were seen in the shaded region and are marked with red arrows. The ROT value for the second blob was higher than the patches (5 TECU/min versus 3 TECU/min). These blobs were associated with slightly enhanced scintillations (up to 0.3 rad). The two strong blobs were associated with scintillation pulses, which were slightly later than the two corresponding pulsed auroral intensifications in Figure 2m (in both red and green lines). But the comparable scintillation was also associated with the third BT-1 blob (up to 0.2 rad) during weak auroral conditions (≤1 kR).

3.1.4. Satellite PRN25

Figures 2n, 2p, and 2r show measurements associated with PRN25. PRN25 was in the southwest of the field of view and slowly moved eastward and attained its highest elevation angle (60°) at 23:00 UT. Four humps in TEC were seen before 22:30 UT. The first part of the following TEC hump (increasing part) is a polar cap patch, while the decreasing part in the shaded region is a BT-1 blob since it was in the auroral region. Later on, three more blobs were observed. The ROT values within the blobs are almost comparable with the polar cap patches. Sporadic scintillations were observed with polar cap patches before 22:38 UT, but the level was generally low (<0.2 rad). After the aurora intersected with the ray path, the scintillation level increased dramatically. The scintillations were seen both in the leading and trailing edges of these blobs, but again lagged behind the auroral intensification pulses. After 23:10 UT, another weak TEC hump (polar cap patch) was observed, but only minor scintillation (0.1 rad) was associated with it.

3.1.5. Short Summary

From this BT-1 case (i.e., when the high-density *F* region polar cap patches enter the auroral region), it is clear that (1) when patches entered the auroral region, GPS phase scintillations (σ_ϕ) were significantly enhanced; (2) although density gradients associated with polar cap patches can be observed from the GPS TEC and ROT, scintillations were not always associated with TEC gradients (see Figures 2i and 2k), i.e., there is not always a good correlation between σ_ϕ and ROT; (3) the scintillation level of BT-1 blobs was not correlated with the scintillation level of patches poleward of the aurora; (4) during the substorm expansion phase, the precipitation ionized the electron density below 200 km altitude; however, the enhancements of T_e was observed above 200 km, while the enhanced T_i was observed down to 120 km and was more obvious above 200 km, and the ion upflow event was also observed in this case.

3.2. BT-2 Blob: 13 January 2013

This case presents the scintillation and ionospheric conditions associated with BT-2 blobs produced by local auroral precipitation only. This case was also used by *Jin et al.* [2014] as an example of strong auroral arcs which were not associated with significant scintillations. In this section, we present a more detailed scintillation picture of this event. We choose to use the available colocated LYR5 ASI and the GNSS receiver in Longyearbyen since they coordinate better with the ESR which is also located in Longyearbyen.

An overview of this case is displayed in Figure 3 in a similar format as in Figure 1. A substorm started around 14:00 UT with the *AL* index reaching its minimum of −600 nT slightly before 16:00 UT and then began to recover until 17:00 UT (not shown in Figure 3). Figures 3a and 3b show optical emissions in a keogram format at 630.0 nm and 557.7 nm from the LYR5 ASI data. The aurora was observed from 14:00 to 18:00 UT and almost covered the entire field of view from 16:00 to 17:30 UT. This is most clear in Figure 3b. Therefore, we focus on the time between 16:00 and 17:00 UT (~19:10 and 20:10 MLT) which, according to the *AL* index, may be termed as the recovery phase of a substorm. The airglow polar cap patches were not seen to move

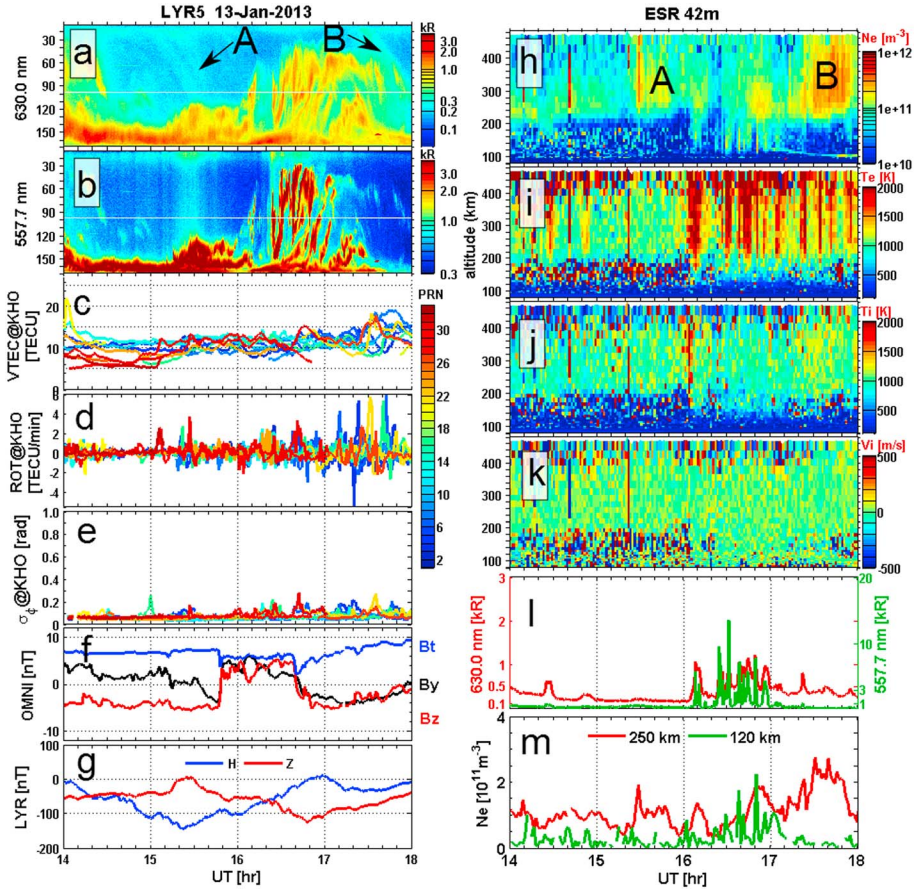

Figure 3. Event overview of the BT-2 case. The format is the same as in Figure 1 but for 13 January 2013. The ASI and GNSS receiver are from Longyearbyen.

equatorward except around 15:10 UT and 17:30 UT, which are annotated by black arrows and are labeled by "A" and "B" in Figure 3a.

Figures 3c and 3d show the GPS TEC and ROT data from KHO in Longyearbyen, respectively. The TEC values were very low before 17:20 UT. Small TEC fluctuations were observed from 15:00 to 17:00 UT in association with the aurora. These TEC fluctuations are due to BT-2 blobs. The pulsed TEC variations are better depicted by the ROT data in Figure 3d. After 17:20 UT, the slow and large TEC variation was associated with polar cap patch B as seen in Figure 3a, and the associated ROT increased dramatically.

The phase scintillation indices (σ_ϕ) from all tracked GPS satellites are shown in Figure 3e. The scintillations were at the noise level before 16:10 UT. After 16:10 UT, the scintillations slightly intensified to 0.2–0.3 rad. Some of these scintillations were associated with the auroral dynamics at this time. However, the highest phase scintillations (up to 0.3 rad) from PRN30 (in red) were associated with the polar cap patches in the north of the field of view (not patches A and B). As these polar cap patches were convected antisunward toward midnight, they did not move toward the center of the ASI field of view. These patches can only be seen by the satellites in the northern part of the field of view such as PRN30.

Figure 3f shows the IMF data from the OMNI data set. IMF B_z was negative except in the period from 15:50 UT to 16:40 UT. The B_y component decreased gradually from 3 nT at 14:00 UT to −3 nT at 15:50 UT, followed by a sharp positive transition. Then B_y decreased again to negative values at 16:40 UT and stayed negative until 18:00 UT. The IMF strength B_t was very stable except during two transition periods around 15:50 UT and around 16:40 UT.

Similar to the previous case, we present the local magnetic data from LYR in Figure 3g. The *H* component decreased from 14:00 UT until 15:20 UT followed by a slow recovery. The *Z* component was generally negative and varied in association with the *H* component.

Figures 3h–3k present electron density (N_e), electron temperature (T_e), and ion temperature (T_i), line of sight ion velocity (V_i) measured with the ESR 42 m dish. The *F* region electron density was generally low except for two intervals around 15:30 UT and 17:50 UT. These were polar cap patches A and B, which can also be seen in Figure 3a. The signature of patch B around 17:50 UT is clearer. The *E* region electron density was very low except for the interval from around 16:00 UT to 17:00 UT. These enhanced electron densities are termed BT-2 blobs since they were locally produced by particle precipitation when the aurora moved into the ESR beam. The electron temperature enhancements were clearly associated with the *E* region ionization. Similar to Figure 1, the electron temperature enhancements were only clearly seen above an altitude of 200 km. The ion temperature was generally unaffected except for the time around 16:05 UT. Unlike Figure 1, ion upflow was not seen in the precipitation region, which was probably due to the unaffected T_i (i.e., no Joule heating). Note that the altitude range was low (up to 480 km) in this experiment.

Figure 3l shows the 630.0 nm (in red) and 557.7 nm (in green) emissions at the ESR beam (the horizontal white lines in Figures 3a and 3b). The auroral emissions were most clear from 16:00 to 17:00 UT with the red line emission up to 1 kR and the green line emission up to 13 kR. The emissions in the ESR beam were quite pulsed which indicate that the aurora was very structured and/or moved rapidly.

Figure 3m shows the electron density at 250 km (*F* region) and 120 km (*E* region) from 14:00 to 18:00 UT derived from ESR measurements. Apart from polar cap patches A and B, the *F* region density was low at $0.5–1 \times 10^{11}$ m^{-3}, while the *E* region density was even lower ($N_e \leq 0.5 \times 10^{11}$ m^{-3}) except between 16:20 UT and 17:00 UT. The *E* region density reached above 2×10^{11} m^{-3} at 16:51 UT, but the *E* region density was very short-lived and decayed to the background value within a minute when the aurora moved away.

Next we present the auroral morphology and the associated scintillation condition in Figure 4. Figures 4a–4f show six snapshots of the auroral images in the green line. The aurora shown in Figures 4a–4f may be the westward traveling surge (WTS) in the evening [*Akasofu*, 1964; *Akasofu et al.,* 1965]. The aurora entered the field of view from the southeast (Figure 4a) and propagated northwestward very rapidly. As the aurora propagated, it rotated clockwise and became quite irregular. The aurora changed its form very quickly and evolved across the whole sky, from patchy-like (Figure 4c) to swirl (Figure 4d), and then broke up into multiple arcs (Figure 4f).

Similar to the case describing BT-1 blobs, we select four GPS satellites to show the scintillation condition associated with BT-2 blobs.

3.2.1. Satellite PRN5

PRN5 was located in the western part of the field of view and moved slowly southeastward. The TEC was stable before 16:30 UT. The fast moving aurora came into and went away from the ray path very quickly, which resulted in a signature of multiple pulses in the optical data at the location of PRN5 from 16:30 to 17:25 UT. At this time, the red line emission went up to 1 kR, while the green line emission went up to 9 kR. The fluctuating TEC with amplitude of 1–2 TECU was recorded and is termed BT-2 blobs. The ROT variation reached up to 2 TECU/min. However, the associated scintillations remained below 0.1 rad throughout this period. From around 17:27 UT, polar cap patch B was seen as a slow increase and decrease of TEC. The scintillations associated with polar cap patch B approached 0.1 rad, but they can still be regarded as insignificant scintillation.

3.2.2. Satellite PRN7

PRN7 was in the southern part of the field of view and slowly moved northeastward. One strong auroral feature passed the ray path at 16:25 UT with green line emissions up to 15 kR. The TEC responded to the aurora and so did the ROT data, but the scintillation index remained unaffected. Polar cap patch B was seen from 17:20 UT and the associated scintillations fluctuated around 0.1 rad, which can be regarded as weak scintillations.

3.2.3. Satellite PRN13

PRN13 was in the southeast part of the field of view in Figure 4a, and then it moved farther southeastward. The aurora near the location of PRN13 was stronger than that of PRN5 and PRN7. The red line emission was up to 1.2 kR, while the green line emission was up to 20 kR. The TEC fluctuations were associated with the auroral form passage through the ray path. The ROT varied between -2 and 2 TECU/min. There was only one point with σ_ϕ larger than 0.1 rad at 16:27 UT. After ~17:00 UT, there was a slight increase of σ_ϕ because PRN13 was at low elevation angle at this time.

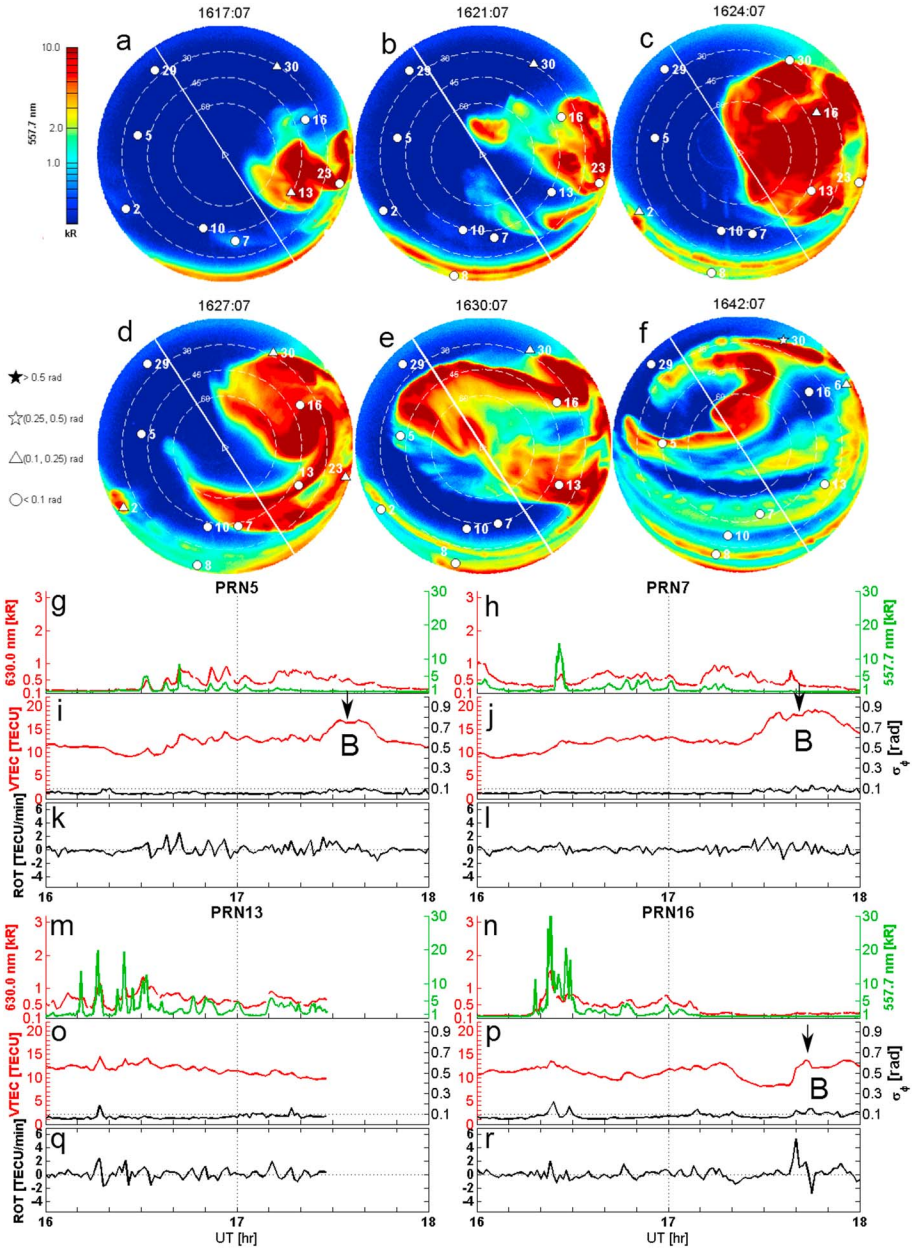

Figure 4. The same format as in Figure 2 but for 13 January 2013. (a–f) A sequence of snapshots showing the dynamical variation of auroral forms. The images are from the 557.7 nm channel. In Figures 4a–4f, the data are presented in the azimuth and elevation angle format. (g–r) Optical emissions, the GPS TEC, ROT, and phase scintillation index for four selected satellites (see text for more details).

3.2.4. Satellite PRN16

PRN16 was in the eastern part of the field of view in Figure 4a and moved slowly northeastward. Strong aurora was seen from 16:18 UT to 16:32 UT with the green line emission up to 30 kR. The TEC fluctuated in response to this aurora and enhanced ROT fluctuations were observed. The σ_ϕ reached 0.2 rad due to the auroral precipitation. Polar cap patch B was seen from 17:38 UT as the TEC suddenly increased, and ROT increased dramatically to 5 TECU/min. Weak scintillations (~0.1 rad) were associated with polar cap patch B.

3.2.5. Short Summary

From this BT-2 blob case, we find that (1) even though the aurora did produce electron density enhancements which are termed BT-2 blobs and caused TEC fluctuations as well as the ROT activity, the phase scintillation level (σ_ϕ) remained low; (2) the aurora was more pulsed at the ESR location than that shown in

section 3.1 due to the fast motion and quickly deformed auroral morphology; (3) the electron density was enhanced down to 100 km altitude due to the particle ionization; (4) the electron temperature was affected by particle precipitation; however, the ion temperature was generally unaffected and ion upflow was not observed; (5) the stable Ti may be due to the fast-moving aurora when the frictional heating only occurs at a short time interval along the auroral boundary as compared to the relatively long interval of auroral precipitation in section 3.1; (6) note that the auroral intensity at the ESR beam reached 1 kR at 630.0 nm and 13 kR at 557.7 nm; however, in the west of the field of view, the auroral intensity reached 1.5 kR at 630.0 nm and 30 kR at 557.7 nm near the location of PRN16 (Figure 4).

4. Statistical Study

In order to evaluate whether it is a general observation that the BT-1 blob is associated with higher scintillation levels than the corresponding polar cap patch and the BT-2 blob, we perform a statistical study with a larger data set. We use the colocated GNSS scintillation receiver and NYA4 ASI in Ny-Ålesund because they have acquired a larger database than the instruments in Longyearbyen. We screened the NYA4 ASI from November 2010 to February 2014 to find clear sky observations. Because the MLT when polar cap patches hit the nightside auroral boundary ranges from 18:30 to 04:50 MLT [*Moen et al.,* 2007], the ASI data from 15:00 UT to 03:00 UT (~18:10 to 06:10 MLT) were surveyed. Since we focus on BT-1 blob formation, we search for data when (1) airglow polar cap patches were observed; (2) the substorm aurora came into the field of view of NYA4 ASI; and (3) the aurora covered more than a quarter of the field of view when the aurora reached its highest latitude. This corresponds to fairly strong substorm aurora poleward expansion. In total, we have 41.4 h of data in 16 days when the three previous criteria were satisfied. In order to contrast the BT-1 blob formation scenario, we further screen the ASI data between 15:00 UT and 03:00 UT and select data when (1) aurora was seen; (2) polar cap patches did not move across the aurora, i.e., no BT-1 blob was formed. Although the patches did not interfere with the aurora, the patches might be seen at the northern part of the ASI field of view, e.g., see section 3.2 and Figure 3. 20 h of data in 5 days were obtained to study the scintillation condition with BT-2 blob category.

The GPS satellites were mapped to the ASI data by using the azimuth and elevation angles. The median value of the data in a 5×5 pixel window around the satellite locations were taken as the emission intensity at the location of the satellites.

Figure 5 shows a scatterplot of the scintillation index (σ_ϕ) versus the auroral emission intensity. Figures 5a and 5b show 20 h of data for the BT-2 blob. Figure 5a shows 630.0 nm optical emission intensity versus σ_ϕ. In general, the scintillations were low, and there is no clear relationship between the scintillation level and the auroral emission intensity, i.e., the high auroral emission intensity does not imply high scintillation level. It should be noted that the scintillations of $\sigma_\phi \sim 0.3$ rad may be caused by the polar cap patches passing through the north part of the ASI field of view when the airglow patches were not moving toward the aurora as shown in section 3.2 by PRN30. However, it is not possible to discriminate the data points one by one. Figure 5b shows results for 557.7 nm optical emissions in the same format as in Figure 5a. Apparently, there is no relationship between σ_ϕ and the 557.7 nm emission intensity, neither.

The 41.4 h of BT-1 blob data are further divided into 26 intervals. One interval is defined by the time starting from when the aurora came into the field of view until it retreated equatorward of the southern horizon or when patches stopped moving into the aurora. This is because when the aurora was active, the polar cap patches can be continuously pulled into the nightside aurora. Once the patches are pulled into the aurora, it is hard to predict their trajectory and locations, and thus, it is impossible to distinguish between different BT-1 blobs.

For each of the 26 intervals of the BT-1 blob formation, we estimate the highest emission intensity of the airglow patches at 630.0 nm before they entered the auroral region. These highest emission values were set to be the upper threshold of the airglow patches. If the optical emission at the satellite location was higher than this threshold, it must be inside the auroral region; otherwise, the satellite must be in the polar cap (either in a polar cap patch or in the background). Since the intensity of nightside aurora seen from Ny-Ålesund was usually very strong ($\geq$1 kR at 630.0 nm), the emission intensity of airglow patches is easily distinguishable from the aurora.

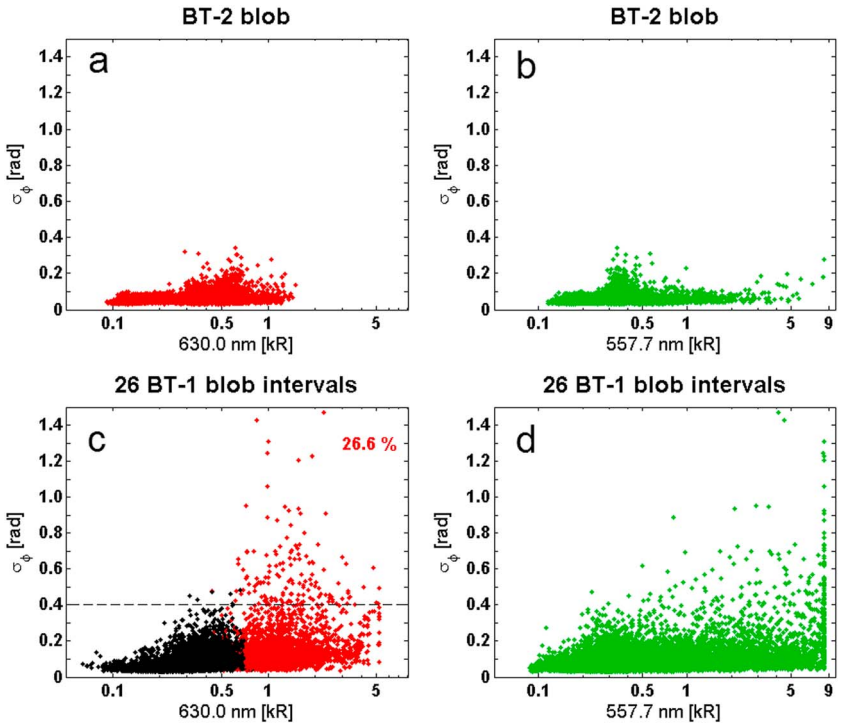

Figure 5. (a) The scatterplot of σ_ϕ versus the auroral emission intensity at 630.0 nm from 20 h of data for the auroras without patches (i.e., BT-2 blobs). (b) The same as Figure 5a but for 557.7 nm. (c) A scatterplot of data in 41.4 h for auroras with patches (i.e., BT-1 blobs). The red dots indicate that measurements were from the auroral region, while the black dots indicate that measurements were in the polar cap (from patches or background). The 26.6% in the top right is the scintillation occurrence rate of $\sigma_\phi > 0.4$ rad in the auroral region. (d) The same as Figure 5c but for 557.7 nm.

Figure 5c shows the scatterplot from 41.4 h of data when the patches hit the aurora (i.e., BT-1 blob formation). The red dots indicate that the measurements are inside the aurora, while the black ones indicate that the data points are in patches or belong to the background. Similar to Figures 5a and 5b, there is no clear relation between scintillation and the auroral emission intensity in Figure 5c. The strong scintillations are mostly between 0.8 and 3 kR, while at high emission intensity (say 5 kR), σ_ϕ can be as low as 0.1 rad. Polar cap patches were associated with scintillation level up to 0.5 rad, while the scintillations inside the auroral region can reach as high as 1.5 rad. The scintillation occurrence rate of $\sigma_\phi > 0.4$ rad in the auroral region is 26.6%. This corresponds to the red dots above the dashed horizontal line in Figure 5c.

Next we compare the statistics of BT-1 blobs with BT-2 blobs (Figures 5c versus 5a). Note that there are more data points in Figure 5c and the range of the auroral emission intensity in Figure 5c (up to 5 kR) is also higher than that in Figure 5a (up to 1.5 kR). However, by comparing those data points which are below 1.5 kR in Figure 5c with Figure 5a, several strong scintillations (up to 1.4 rad) with moderate auroral intensity (around 1 kR) are already observed. This indicates that the auroral emission intensity is not the only reason for scintillation production. Thus, the upper limit of the auroral intensity in Figure 5a does not affect our comparison of Figure 5c (BT-1 blobs) with Figure 5a (BT-2 blobs). From Figures 5a and 5c, it is clear that BT-1 blobs are associated with higher scintillation level than BT-2 blobs.

Figure 5d presents a scatterplot of σ_ϕ versus 557.7 nm data in a similar format as Figure 5c. The NYA4 ASI saturates at 9 kR in the 557.7 nm channel. In the intensity calibration of the ASI, a linear relation between kilo Rayleigh and the counts was assumed. This assumption is valid away from the saturation region; however, around the saturation region the relation can be far from linear. We find that 9 kR in NYA4 ASI may correspond to 30 kR in LYR5 ASI. Despite the saturation of the 557.7 nm channel, no clear relation was seen between the scintillation and the auroral emission intensity.

In order to compare the scintillation level of a polar cap patch and the BT-1 blob, we show the highest scintillation value before and after patches entering the aurora in these 26 intervals.

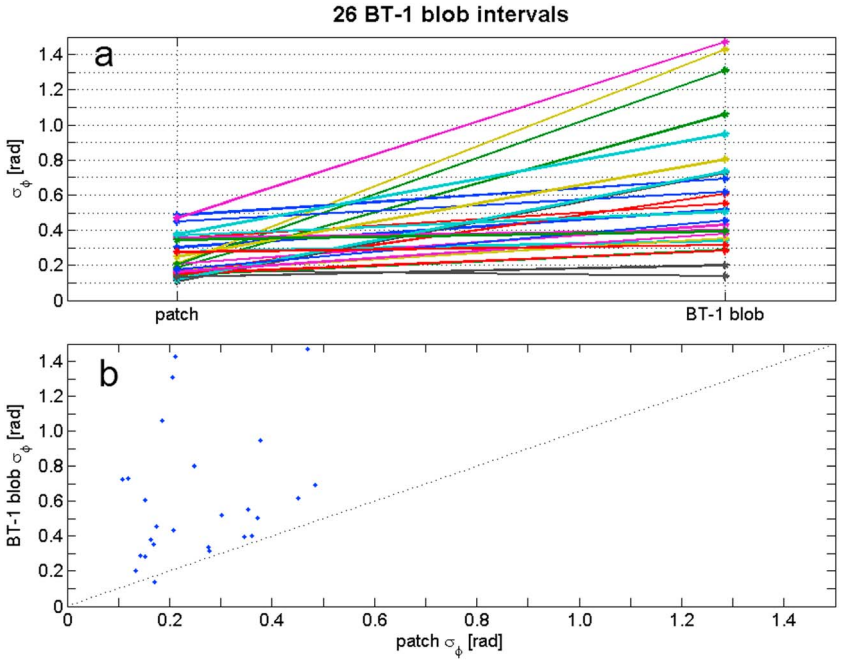

Figure 6. (a) For each of the 26 BT-1 blob intervals, the highest scintillation index before patches entering the auroral region is shown on the left, while the highest scintillation index after patches entering the auroral region is shown on the right. (b) A scatterplot showing the highest scintillation associated with patches and BT-1 blobs.

Figure 6a shows the highest σ_ϕ in patches on the left and the highest σ_ϕ inside the auroral region with a line connecting them for each of the 26 intervals. Although we are unable to separate the contribution to scintillations from the aurora or patches or their interaction, we still refer to the right side as the BT-1 blob group. This is because it was demonstrated in section 3.2 and in Figures 5a and 5b, that the aurora alone did not produce strong scintillation; therefore, the highest scintillation should be associated with the BT-1 blob. For 25 out of 26 cases, the scintillation level was enhanced when the patch entered the auroral region. There was only one exception when the patch entered the aurora, the scintillation decreased. In this exceptional case, the scintillation levels on both sides were very low (around 0.15 rad).

Figure 6b shows the scatterplot of BT-1 blob scintillation index and patch scintillation index. The slant dotted line shows $y = x$. Therefore, the data points above this line show the enhanced scintillation after patches enter into the auroral region, and vice versa. Only one point shows a decrease from 0.18 rad to 0.15 rad. The highest scintillation level for the patches ranges from 0.1 to 0.5 rad. Four blobs lie above 1 rad, 10 blobs are between 0.5 and 1 rad, and 12 blobs are between 0.1 and 0.5 rad. There is no clear functional relationship between σ_ϕ in patches and in BT-1 blobs, which indicates that the scintillation condition of BT-1 blobs (the combination of the aurorae and patches) is independent of the prestructures in patches. Therefore, it is likely that the auroral dynamics plays an important role in the further structuring of the BT-1 blobs.

5. Discussion

In order to differentiate the scintillation effect of the aurora and *F* region polar cap patches, we defined two types of blobs: BT-1 and BT-2. First, we presented the scintillation picture of polar cap patches exiting the polar cap on 1 February 2014 by combining the ASI, ESR, GPS TEC, and σ_ϕ. Results show that once the polar cap patches entered the auroral region, the enhanced scintillation level was associated with BT-1 blobs. However, the scintillation level of BT-1 blobs was uncorrelated with the scintillation level of each patch. During this event, ESR measured ionization below 200 km due to particle precipitation but the electron density at altitudes above 200 km was generally unaffected. We further presented the scintillation picture of a pure aurora case (without polar cap patches entering into the aurora) and studied BT-2 blobs on 13 January 2013 by a similar set of instruments. The aurora produced electron density enhancements mainly from 100 to 200 km and GPS TEC fluctuations; however, the associated scintillations were insignificant. Note

that in the latter case the aurora was observed in the late evening (19:30–20:00 MLT), while the BT-1 case was observed at postmidnight (1:00–2:00 MLT), the auroral intensity in the BT-2 case was still comparable to that in the BT-1 case. The similar auroral intensities but significantly different scintillation levels indicate the importance of the *F* region BT-1 blobs in producing scintillations.

To test the representativeness of the two cases shown in section 3, here, for the first time, we presented a statistical study of the scintillation condition associated with BT-1 and BT-2 blobs. We require observations of both polar cap patches and the aurora at the same time and require the area of the aurora to be large enough to have statistical significance (i.e., enough data points in the auroral region), and with these requirements, 41.4 h of data in total were obtained in 3.5 years. 20 h of BT-2 data were also obtained in the same 3.5 years. The most striking result is that there is no clear correlation between σ_ϕ and the auroral emission intensity, i.e., high auroral intensity does not necessarily indicate high σ_ϕ. Furthermore, the statistical results of 41.4 h of BT-1 data and 20 h of BT-2 data agree with the results of the two case studies, i.e., BT-1 blob is associated with higher scintillation level than the corresponding polar cap patch and the BT-2 blob. There is no clear relationship between the scintillation level between patches and the resulting BT-1 blobs (see Figure 6). This indicates that in addition to the preexisting irregularities in the patches, the auroral dynamics (intensity and/or morphology) play an important role in structuring BT-1 blobs.

The poor correlation between σ_ϕ and the auroral emission intensity in our study is different from the conclusion of *Kinrade et al.* [2013], which found correlation levels of up to 74% during 2 h of discrete arc structuring using data from the South Pole Station. Since their ASI was unable to track the weak airglow from polar cap patches, they did not consider any contribution to scintillations from *F* region polar cap patches. Although the correlation between the auroral emission intensity and σ_ϕ could be high in a short observation period when there are no polar cap patches, a close look at their Figure 6 indicates that the auroral brightening does not always correspond to simultaneous pulses of intensified scintillations, and a higher auroral intensity does not always correspond to higher σ_ϕ. If one studied the scintillation and aurora data over a longer time period, their correlation will most likely be degraded due to the highly varying ionospheric background (e.g., electron density variations from transient events like polar cap patches, storm-enhanced densities, diurnal variations, and seasonal effects). Indeed, *Kinrade et al.* [2013] also showed poor correlation down to 3% using 8 h of data. Accordingly, a correlation study of scintillations and auroral intensity must also consider the changing background ionosphere.

There are different instability modes which structure BT-1 blobs in the auroral region. Those polar cap patches which are associated with density gradients favor the action of the GDI, and plasma irregularities are produced on the trailing edge [*Keskinen and Ossakow*, 1983; *Milan et al.,* 2002]. After the patch turns into a BT-1 blob, density gradients will be preserved, which means that the GDI, which works on patches, will work on the BT-1 blob as well [*Cerisier et al.,* 1985; *Basu et al.,* 1990]. Furthermore, it has been shown that the velocity shear in the background convection can split the polar cap patch into smaller substructures [*Hosokawa et al.,* 2010]. By the same token, in the vicinity of an auroral arc, the presence of the velocity shear is capable to break the large-scale patches into smaller pieces and create new density gradients. Taking the auroral streamer, for example [see, e.g., *Sergeev et al.,* 2004; *Amm and Kauristie*, 2002, and references therein], the north-south aligned arc is associated with an upward FAC; while on the east there is another downward FAC. The upward and downward FACs set up electric fields as shown by black dashed arrows in Figure 7. The electric field induces plasma drift in the $\mathbf{E} \times \mathbf{B}$ direction which will form an equatorward flow burst between the pair of FACs and flow shears on the west side of the auroral arc and on the east side of the downward FAC. On both sides, the velocity shears can create substructures and new density gradients as also shown in Figure 7a. Therefore, as illustrated in Figure 7b, the velocity shears are likely to drive KHI near the newly created density gradients where the vortex structures are formed and small-scale structures are developed quickly [*Keskinen et al.,* 1988]. Note that the secondary GDI can also work on the large-scale vortex structures. While on the trailing edge of the BT-1 blob, the equatorward flow burst drive GDI which produce finger-like elongated structures [*Gondarenko and Guzdar*, 2004]. Moreover, on the eastside of the BT-1 blob (downward FAC region), in addition to the KHI, the FAC triggers the CCI [*Ossakow and Chaturvedi*, 1979; *Tsunoda*, 1988].

On the other hand, the damping term of the irregularities is also to be considered in the auroral region. The damping term includes diffusion and recombination. The *F* region plasma recombines very slowly on the order of hours and can be neglected. *Vickrey and Kelley* [1982] have established a theory which shows that the cross field diffusion of the *F* region ionosphere is significantly enhanced when it connects to a conducting

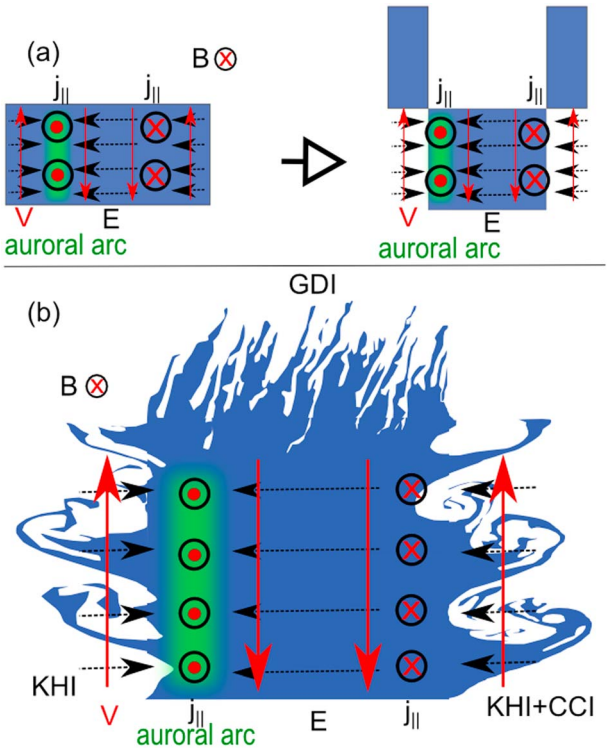

Figure 7. (a) Flow shears cut a polar cap patch into substructures. (b) A schematic illustration of irregularity growth of a BT-1 blob in the nightside auroral region.

E region. Therefore, the lifetime of *F* region irregularities is reduced in the auroral region where the *E* region is formed by particle impact ionization. But the conducting *E* region cannot prevent the instabilities from operating on the *F* region plasma, i.e., the underlying auroral *E* layer may not completely inhibit the irregularity formation [*Weber et al.,* 1985]. The fast decay means a lack of memory in the power of irregularities, i.e., when a BT-1 blob is formed in the auroral oval, its accompanying irregularities are determined by the local production and decay, and therefore, there is no correlation in the scintillation level between the BT-1 blob and the corresponding patch.

In the recent case study by *van der Meeren et al.* [2015], the strongest GNSS phase scintillation region was found at the poleward part of the nightside auroral region during the formation of BT-1 blobs. As it was discussed earlier, various instabilities can explain the higher scintillation level associated with BT-1 blobs than the prior polar cap patches, while the auroral *E* region may explain the fast damping of plasma irregularities at the equatorward part of the auroral oval. More observations and theoretical studies are needed to resolve the exact mechanisms which enhance and damp the power of irregularities.

Another relevant and important process for *F* region irregularity production is the soft particle precipitation [*Kelley et al.,* 1982]. *Kelley et al.* [1982] suggested that much of large-scale structures in the high-latitude *F* region are caused by soft particle precipitation. The situation in the dayside cusp region was verified by the ICI-2 rocket studies [*Moen et al.,* 2012; *Spicher et al.,* 2014, 2015b]. However, it may not be the case in the nigthside auroral oval during a substorm. By using the Poker Flat incoherent scatter radar, *Nishimura et al.* [2014] found that during the growth phase of a substorm, the precipitation ionized altitudes from 200 km to 300 km, while during the expansion phase of the substorm, the precipitation mainly affected altitudes below 200 km. Since our measurements were taken on Svalbard, which is poleward of the nightside auroral oval for most of the time, we investigate the substorm expansion phase when the aurora expanded poleward enough to be seen by the ASI. From the ESR measurements in section 3, we see that the particle impact ionization occurred at altitudes below 200 km and peaked around 110 km. However, the electron temperature is enhanced above the altitude of 200 km as a result of precipitation and the ion temperature was enhanced as a result of ion frictional heating which results in ion upwelling. We are unable to resolve whether these secondary effects (following enhanced T_e, T_i, and upward V_i) could affect the *F* region structure. To conclude, during the substorm expansion phase, the soft particle precipitation in the northern edge of the auroral oval cannot explain the strongly enhanced scintillation. In order to fully understand the physics behind the strong scintillation associated with BT-1 blobs, multiscale and multipoint in situ measurements are needed.

6. Summary

1. This study clearly shows that the scintillation level of the BT-1 blob is higher than the scintillation level of the corresponding patch and the BT-2 blob. The aurora alone (i.e., BT-2 blob) did not produce significant scintillations. Whenever patches exit into the auroral region, the scintillation level will be intensified, and the highest scintillation level is inside the nightside auroral region.

2. There is no clear relationship between the BT-1 blobs scintillation and the preconditioning scintillation level of the polar cap patches. This can be explained by the lack of memory in the irregularities power caused by the fast damping of the irregularities when there is a conducting auroral *E* region. However, the higher scintillation level with BT-1 blobs implies that the plasma dynamics in connection with auroral arcs play a key role in intensifying the BT-1 blob scintillation level.
3. At the nightside auroral region, soft particle precipitation as proposed by *Kelley et al.* [1982] is unlikely to be the main source of large-scale *F* region plasma structures and therefore cannot explain the enhanced scintillation with BT-1 blobs.

Acknowledgments
The authors thank the Norwegian Polar Research Institute at Ny-Ålesund for assisting us with the GPS receiver and the optical observations in Ny-Ålesund, Kjell Henriksen Observatory (KHO) for LYR5 ASI operation, Bjørn Lybekk and Espen Trondsen for the instrument operations, and Charles Carrano for providing the GPS software. Yaqi Jin thanks Steve Milan for discussions. The research has received financial support from the Research Council of Norway grant 230996. This research is a part of the 4DSpace Strategic Research Initiative at the University of Oslo. The imagers at NYA and LYR are supported by Research Council of Norway under contract 230935. The imager data are available at http://tid.uio.no/plasma/aurora/. The NovAtel GPStation 6 receiver at the KHO in Longyearbyen is supported by the Research Council of Norway under contracts 212014 and 223252, and the data may be obtained from Kjellmar Oksavik (e-mail: kjellmar.oksavik@uib.no). The IMF data are provided by the NASA OMNIWeb service (http://omniweb.gsfc.nasa.gov). The Longyearbyen (LYR) magnetometer data are provided by Tromsø Geophysical Observatory, the Arctic University of Norway (UiT), and are available from http://flux.phys.uit.no/ascii. EISCAT is an international association supported by research organizations in China (CRIRP), Finland (SA), Japan (NIPR and STEL), Norway (NFR), Sweden (VR), and the United Kingdom (NERC). Data from EISCAT can be obtained from the Madrigal database http://www.eiscat.se/madrigal. The authors wish to thank the reviewers for their valuable comments to improve the paper.

References

Aarons, J. (1982), Global morphology of ionospheric scintillations, *Proc. IEEE*, *70*(4), 360–378.
Aarons, J., J. A. Klobuchar, H. E. Whitney, J. Austen, A. L. Johnson, and C. L. Rino (1983), Gigahertz scintillations associated with equatorial patches, *Radio Sci.*, *18*(3), 421–434, doi:10.1029/RS018i003p00421.
Akasofu, S.-I. (1964), The development of the auroral substorm, *Planet. Space Sci.*, *12*, 273–282, doi:10.1016/0032-0633(64)90151-5.
Akasofu, S.-I., D. S. Kimball, and C.-I. Meng (1965), The dynamics of the aurora—II: Westward traveling surges, *J. Atmos. Terr. Phys.*, *27*(2), 173–187, doi:10.1016/0021-9169(65)90114-5.
Alfonsi, L., L. Spogli, G. De Franceschi, V. Romano, M. Aquino, A. Dodson, and C. N. Mitchell (2011), Bipolar climatology of GPS ionospheric scintillation at solar minimum, *Radio Sci.*, *46*, RS0D05, doi:10.1029/2010RS004571.
Amm, O., and K. Kauristie (2002), Ionospheric signatures of bursty bulk flows, *Surv. Geophys.*, *23*, 1–32, doi:10.1023/A:1014871323023.
Andalsvik, Y. L., and K. S. Jacobsen (2014), Observed high-latitude GNSS disturbances during a less-than-minor geomagnetic storm, *Radio Sci.*, *49*, 1277–1288, doi:10.1002/2014RS005418.
Basu, S., and Groves, K. M. (2001) Specification and forecasting of outages on satellite communication and navigation systems, in *Space Weather*, edited by P. Song, H. J. Singer, and G. L. Siscoe, AGU, Washington, D. C. doi: 10.1029/GM125p0423.
Basu, S., E. Mackenzie, and S. Basu (1988), Ionospheric constraints on VHF/UHF communications links during solar maximum and minimum periods, *Radio Sci.*, *23*, 363–378, doi:10.1029/RS023i003p00363.
Basu, S., S. Basu, E. Mackenzie, W. R. Coley, J. R. Sharber, and W. R. Hoegy (1990), Plasma structuring by the gradient drift instability at high-latitudes and comparison with velocity shear driven processes, *J. Geophys. Res.*, *95*, 7799–7818, doi:10.1029/JA095iA06p07799.
Basu, S., K. M. Groves, S. Basu, and P. J. Sultan (2002), Specification and forecasting of scintillations in communication/navigation links: Current status and future plans, *J. Atmos. Sol. Terr. Phys.*, *64*(16), 1745–1754.
Blanchard, G. T., L. R. Lyons, J. C. Samson, and F. J. Rich (1995), Locating the polar cap boundary from observations of 6300 Angstrom auroral emission, *J. Geophys. Res.*, *100*, 7855–7862, doi:10.1029/94JA02631.
Buchau, J., E. J. Weber, D. N. Anderson, H. C. Carlson, J. G. Moore, B. W. Reinisch, and R. C. Livingston (1985), Ionospheric structures in the polar-cap—Their origin and relation to 250 Mhz scintillation, *Radio Sci.*, *20*, 325–338, doi:10.1029/RS020i003p00325.
Carlson, H. C. (2012), Sharpening our thinking about polar cap ionospheric patch morphology, research, and mitigation techniques, *Radio Sci.*, *47*, RS0L21, doi:10.1029/2011RS004946.
Carrano, C. S., A. Anghel, R. A. Quinn, and K. M. Groves (2009), Kalman filter estimation of plasmaspheric total electron content using GPS, *Radio Sci.*, *44*, RS0A10, doi:10.1029/2008RS004070.
Cerisier, J. C., J. J. Berthelier, and C. Beghin (1985), Unstable density gradients in the high-latitude ionosphere, *Radio Sci.*, *20*, 755–761, doi:10.1029/RS020i004p00755.
Clausen, L. B. N., J. I. Moen, K. Hosokawa, and J. M. Holmes (2016), GPS scintillations in the high latitudes during periods of dayside and nightside reconnection, *J. Geophys. Res. Space Physics*, *121*, doi:10.1002/2015JA022199, in press.
Crowley, G., A. J. Ridley, D. Deinst, S. Wing, D. J. Knipp, B. A. Emery, F. Foster, R. Heelis, M. Hairston, and B. W. Reinisch (2000), Transformation of high-latitude ionospheric *F* region patches into blobs during the March 21, 1990, storm, *J. Geophys. Res.*, *105*, 5215–5230, doi:10.1029/1999JA900357.
Foster, J. C., et al. (2005), Multiradar observations of the polar tongue of ionization, *J. Geophys. Res.*, *110*, A09S31, doi:10.1029/2004JA010928.
Fremouw, E. J., R. L. Leadabrand, R. C. Livingston, M. D. Cousins, C. L. Rino, B. C. Fair, and R. A. Long (1978), Early results from DNA wideband satellite experiment: Complex-signal scintillation, *Radio Sci.*, *13*, 167–187, doi:10.1029/RS013i001p00167.
Gondarenko, N. A., and P. N. Guzdar (2004), Plasma patch structuring by the nonlinear evolution of the gradient drift instability in the high-latitude ionosphere, *J. Geophys. Res.*, *109*, A09301, doi:10.1029/2004JA010504.
Hey, J. S., S. J. Parsons, and J. W. Phillips (1946), Fluctuations in cosmic radiation at radiofrequencies, *Nature*, *158*(4007), 234–234.
Hosokawa, K., K. Shiokawa, Y. Otsuka, T. Ogawa, J. P. St-Maurice, G. J. Sofko, and D. A. Andre (2009), Relationship between polar cap patches and field-aligned irregularities as observed with an all-sky airglow imager at Resolute Bay and the PolarDARN radar at Rankin Inlet, *J. Geophys. Res.*, *114*, A03306, doi:10.1029/2008JA013707.
Hosokawa, K., J.-P. St-Maurice, G. J. Sofko, K. Shiokawa, Y. Otsuka, and T. Ogawa (2010), Reorganization of polar cap patches through shears in the background plasma convection, *J. Geophys. Res.*, *115*, A01303, doi:10.1029/2009JA014599.
Hosokawa, K., J. I. Moen, K. Shiokawa, and Y. Otsuka (2011), Decay of polar cap patch, *J. Geophys. Res.*, *116*, A05306, doi:10.1029/2010JA016297.
Huba, J. D., A. B. Hassam, I. B. Schwartz, and M. J. Keskinen (1985), Ionospheric turbulence: Interchange instabilities and chaotic fluid behavior, *Geophys. Res. Lett.*, *12*, 65–68, doi:10.1029/GL012i001p00065.
Hudson, M. K., and M. C. Kelley (1976), The temperature gradient drift instability at the equatorward edge of the ionospheric plasma trough, *J. Geophys. Res.*, *81*, 3913–3918, doi:10.1029/JA081i022p03913.
Jin, Y., J. I. Moen, and W. J. Miloch (2014), GPS scintillation effects associated with polar cap patches and substorm auroral activity: Direct comparison, *J. Space Weather Space Clim.*, *4*, A23, doi:10.1051/swsc/2014019.
Jin, Y., J. I. Moen, and W. J. Miloch (2015), On the collocation of the cusp aurora and the GPS phase scintillation: A statistical study, *J. Geophys. Res. Space Physics*, *120*, 9176–9191, doi:10.1002/2015JA021449.
Kelley, M. C., K. D. Baker, J. C. Ulwick, C. L. Rino, and M. J. Baron (1980), Simultaneous rocket probe, scintillation, and incoherent scatter radar observations of irregularities in the auroral zone ionosphere, *Radio Sci.*, *15*, 491–505, doi:10.1029/RS015i003p00491.
Kelley, M. C., J. F. Vickrey, C. W. Carlson, and R. Torbert (1982), On the origin and spatial extent of high-latitude *F* region irregularities, *J. Geophys. Res.*, *87*, 4469–4475, doi:10.1029/JA087iA06p04469.

Keskinen, M. J., H. G. Mitchell, J. A. Fedder, P. Satyanarayana, S. T. Zalesak, and J. D. Huba (1988), Nonlinear evolution of the Kelvin-Helmholtz instability in the high-latitude ionosphere, *J. Geophys. Res.*, *93*, 137–152, doi:10.1029/JA093iA01p00137.

Keskinen, M. J., and S. L. Ossakow (1983), Theories of high-latitude ionospheric irregularities: A review, *Radio Sci.*, *18*, 1077–1091, doi:10.1029/RS018i006p01077.

King, J. H., and N. E. Papitashvili (2005), Solar wind spatial scales in and comparisons of hourly Wind and ACE plasma and magnetic field data, *J. Geophys. Res.*, *110*, A02104, doi:10.1029/2004JA010649.

Kinrade, J., C. N. Mitchell, N. D. Smith, Y. Ebihara, A. T. Weatherwax, and G. S. Bust (2013), GPS phase scintillation associated with optical auroral emissions: First statistical results from the geographic South Pole, *J. Geophys. Res. Space Physics*, *118*, 2490–2502, doi:10.1002/jgra.50214.

Kintner, P. M., B. M. Ledvina, and E. R. de Paula (2007), GPS and ionospheric scintillations, *Space Weather*, *5*, S09003, doi:10.1029/2006SW000260.

Kintner, P. M., and C. E. Seyler (1985), The status of observations and theory of high-latitude ionospheric and magnetospheric plasma turbulence, *Space Sci. Rev.*, *41*(1–2), 91–129.

Lorentzen, D. A., N. Shumilov, and J. Moen (2004), Drifting airglow patches in relation to tail reconnection, *Geophys. Res. Lett.*, *31*, L02806, doi:10.1029/2003GL017785.

Milan, S. E., M. Lester, and T. K. Yeoman (2002), HF radar polar patch formation revisited: Summer and winter variations in dayside plasma structuring, *Ann. Geophys.*, *20*, 487–499.

Mitchell, C. N., L. Alfonsi, G. De Franceschi, M. Lester, V. Romano, and A. W. Wernik (2005), GPS TEC and scintillation measurements from the polar ionosphere during the October 2003 storm, *Geophys. Res. Lett.*, *32*, L12S0, doi:10.1029/2004GL021644.

Moen, J., I. K. Walker, L. Kersley, and S. E. Milan (2002), On the generation of cusp HF backscatter irregularities, *J. Geophys. Res.*, *107*(A4), 1044, doi:10.1029/2001JA000111.

Moen, J., N. Gulbrandsen, D. A. Lorentzen, and H. C. Carlson (2007), On the MLT distribution of *F* region polar cap patches at night, *Geophys. Res. Lett.*, *34*, L14113, doi:10.1029/2007GL029632.

Moen, J., K. Oksavik, T. Abe, M. Lester, Y. Saito, T. A. Bekkeng, and K. S. Jacobsen (2012), First in-situ measurements of HF radar echoing targets, *Geophys. Res. Lett.*, *39*, L07104, doi:10.1029/2012GL051407.

Moen, J., K. Oksavik, L. Alfonsi, Y. Daabakk, V. Romano, and L. Spogli (2013), Space weather challenges of the polar cap ionosphere, *J Space Weather Space Clim.*, *3*, A02, doi:10.1051/swsc/2013025.

Moen, J., K. Hosokawa, N. Gulbrandsen, and L. B. N. Clausen (2015), On the symmetry of ionospheric polar cap patch exits around magnetic midnight, *J. Geophys. Res. Space Physics*, *120*, 7785–7797, doi:10.1002/2014JA020914.

Nishimura, Y., et al. (2014), Coordinated ionospheric observations indicating coupling between preonset flow bursts and waves that lead to substorm onset, *J. Geophys. Res. Space Physics*, *119*, 3333–3344, doi:10.1002/2014JA019773.

NovAtel (2012), GPStation-6 GNSS Ionospheric Scintillation and TEC Monitor (GISTM) Receiver User Manual, NovAtel Inc., Calgary, Alberta. [Available at http://www.novatel.com/assets/Documents/Manuals/om-20000132.pdf, Accessed date 24 Feb. 2016.]

Oksavik, K., V. L. Barth, J. Moen, and M. Lester (2010), On the entry and transit of high-density plasma across the polar cap, *J. Geophys. Res.*, *115*, A12308, doi:10.1029/2010JA015817.

Oksavik, K., J. Moen, M. Lester, T. A. Bekkeng, and J. K. Bekkeng (2012), In situ measurements of plasma irregularity growth in the cusp ionosphere, *J. Geophys. Res.*, *117*, A11301, doi:10.1029/2012JA017835.

Oksavik, K., C. van der Meeren, D. A. Lorentzen, L. J. Baddeley, and J. Moen (2015), Scintillation and loss of signal lock from poleward moving auroral forms in the cusp ionosphere, *J. Geophys. Res. Space Physics*, *120*, 9161–9175, doi:10.1002/2015JA021528.

Ossakow, S. L., and P. K. Chaturvedi (1979), Current convective instability in the diffuse aurora, *Geophys. Res. Lett*, *6*, 332–334, doi:10.1029/GL006i004p00332.

Perry, G. W., J.-P. St.-Maurice, and K. Hosokawa (2013), The interconnection between cross-polar cap convection and the luminosity of polar cap patches, *J. Geophys. Res. Space Physics*, *118*, 7306–7315, doi:10.1002/2013JA019196.

Prikryl, P., P. T. Jayachandran, S. C. Mushini, and R. Chadwick (2011), Climatology of GPS phase scintillation and HF radar backscatter for the high-latitude ionosphere under solar minimum conditions, *Ann. Geophys.*, *29*(2), 377–392.

Prikryl, P., P. T. Jayachandran, S. C. Mushini, D. Pokhotelov, J. W. MacDougall, E. Donovan, E. Spanswick, and J. P. S. Maurice (2010), GPS TEC, scintillation and cycle slips observed at high latitudes during solar minimum, *Ann. Geophys.*, *28*(6), 1307–1316.

Rees, M. H. (1963), Auroral ionization and excitation by incident energetic electrons, *Planet. Space Sci.*, *11*, 1209–1218, doi:10.1016/0032-0633(63)90252-6.

Rino, C. L., R. C. Livingston, R. T. Tsunoda, R. M. Robinson, J. F. Vickrey, C. Senior, M. D. Cousins, J. Owen, and J. A. Klobuchar (1983), Recent studies of the structure and morphology of auroral-zone *F* region irregularities, *Radio Sci.*, *18*, 1167–1180, doi:10.1029/RS018i006p01167.

Sandholt, P. E., H. C. Carlson, and A. Egeland (2002), Optical aurora, in *Dayside and Polar Cap Aurora, Astrophysics and Space Science Library*, vol. 270, pp. 33–49, Kluwer, Acad., Dordrecht, Netherlands.

Sergeev, V. A., K. Liou, P. T. Newell, S.-I. Ohtani, M. R. Hairston, and F. Rich (2004), Auroral streamers: Characteristics of associated precipitation, convection and field-aligned currents, *Ann. Geophys.*, *22*, 537–548, doi:10.5194/angeo-22-537-2004.

Spicher, A., W. J. Miloch, and J. I. Moen (2014), Direct evidence of double-slope power spectra in the high-latitude ionospheric plasma, *Geophys. Res. Lett.*, *41*, 1406–1412, doi:10.1002/2014GL059214.

Spicher, A., T. Cameron, E. M. Grono, K. N. Yakymenko, S. C. Buchert, L. B. N. Clausen, D. J. Knudsen, K. A. McWilliams, and J. I. Moen (2015a), Observation of polar cap patches and calculation of gradient drift instability growth times: A swarm case study, *Geophys. Res. Lett.*, *42*, 201–206, doi:10.1002/2014GL062590.

Spicher, A., W. J. Miloch, L. B. N. Clausen, and J. I. Moen (2015b), Plasma turbulence and coherent structures in the polar cap observed by the ICI-2 sounding rocket, *J. Geophys. Res. Space Physics*, *120*, 10,959–10,978, doi:10.1002/2015JA021634.

Spogli, L., L. Alfonsi, G. De Franceschi, V. Romano, M. H. O. Aquino, and A. Dodson (2009), Climatology of GPS ionospheric scintillations over high and mid latitude European regions, *Ann. Geophys.*, *27*(9), 3429–3437.

Tsunoda, R. T. (1988), High-latitude *F* region irregularities: A review and synthesis, *Rev. Geophys.*, *26*, 719–760, doi:10.1029/RG026i004p00719.

van der Meeren, C., K. Oksavik, D. Lorentzen, J. I. Moen, and V. Romano (2014), GPS scintillation and irregularities at the front of an ionization tongue in the nightside polar ionosphere, *J. Geophys. Res. Space Physics*, *119*, 8624–8636, doi:10.1002/2014JA020114.

van der Meeren, C., K. Oksavik, D. A. Lorentzen, M. T. Rietveld, and L. B. N. Clausen (2015), Severe and localized GNSS scintillation at the poleward edge of the nightside auroral oval during intense substorm aurora, *J. Geophys. Res. Space Physics*, *120*, 10,607–10,621, doi:10.1002/2015JA021819.

Van Dierendonck, A. J., J. Klobuchar, and Q. Hua (1993), Ionospheric scintillation monitoring using commercial single frequency C/A code receivers, paper presented at the 6th International Technical Meeting of the Satellite Division of The Institute of Navigation (ION GPS 1993), Salt Lake City, Utah, 22–24 Sept.

Vickrey, J. F., and M. C. Kelley (1982), The effects of a conducting *E* layer on classical *F* region cross-field plasma-diffusion, *J. Geophys. Res.*, *87*, 4461–4468, doi:10.1029/JA087iA06p04461.

Vickrey, J. F., C. L. Rino, and T. A. Potemra (1980), Chatanika/Triad observations of unstable ionization enhancements in the auroral F-region, *Geophys. Res. Lett.*, *7*, 789–792, doi:10.1029/GL007i010p00789.

Weber, E. J., J. A. Klobuchar, J. Buchau, H. C. Carlson, R. C. Livingston, O. Delabeaujardiere, M. Mccready, J. G. Moore, and G. J. Bishop (1986), Polar cap *F* layer patches: Structure and dynamics, *J. Geophys. Res.*, *91*, 12,121–12,129, doi:10.1029/JA091iA11p12121.

Weber, E. J., R. T. Tsunoda, J. Buchau, R. E. Sheehan, D. J. Strickland, W. Whiting, and J. G. Moore (1985), Coordinated measurements of auroral zone plasma enhancements, *J. Geophys. Res.*, *90*, 6497–6513, doi:10.1029/JA090iA07p06497.

Yeh, K. C., and C.-H. Liu (1982), Radio wave scintillations in the ionosphere, *Proc. IEEE*, *704*, 325–378.

Zesta, E., E. Donovan, L. Lyons, G. Enno, J. S. Murphree, and L. Cogger (2002), Two-dimensional structure of auroral poleward boundary intensifications, *J. Geophys. Res.*, *107*(A11), 1350, doi:10.1029/2001JA000260.

Zhang, Q. H., et al. (2013), Direct observations of the evolution of polar cap ionization patches, *Science*, *339*(6127), 1597–1600.

Zhang, Q.-H., M. Lockwood, J. C. Foster, S.-R. Zhang, B.-C. Zhang, I. W. McCrea, J. Moen, M. Lester, and J. M. Ruohoniemi (2015), Direct observations of the full Dungey convection cycle in the polar ionosphere for southward interplanetary magnetic field conditions, *J. Geophys. Res. Space Physics*, *120*, 4519–4530, doi:10.1002/2015JA021172.